Evidence for three-dimensional unstable flows in shear-banding wormlike micelles

Lydiane Bécu,* Domitille Anache, Sébastien Manneville,† and Annie Colin‡
Centre de Recherche Paul Pascal, Avenue Schweitzer, 33600 Pessac, France
(Received 7 November 2006; published 5 July 2007)

We report on an experimental study of the shear-banding phenomenon in the concentrated wormlike micellar system CTAB at 20 wt. % in D_2O. Time-resolved velocity profiles are recorded using ultrasonic velocimetry simultaneously to global rheological data. Our results confirm the studies performed previously by Fischer and Callaghan [Phys. Rev. E **64**, 011501 (2001)]. Time averaged velocity profiles display an unsheared "nematic gel." In the range of applied shear rate, the flow field exhibits very fast temporal fluctuations. Suspicions for the presence of three-dimensional flow are evidenced and possible causes for a three-dimensional instability are discussed together with the coupling of wall slip to bulk dynamic.

DOI: 10.1103/PhysRevE.76.011503 PACS number(s): 83.80.Qr, 83.60.−a, 47.50.−d, 43.58.+z

I. INTRODUCTION

The coupling between the flow and the microstructure of complex fluids is known to induce inhomogeneous flows characterized by the coexistence of bands of different structures and viscosities. This shear-banding phenomenon has been observed in various soft materials such as lyotropic lamellar phases [1], hexagonal phases [2], colloidal crystals [3], copolymer solutions [4], and wormlike micelles [5–8]. Wormlike micellar solutions constitute model systems to study this behavior and have received considerable attention during the last decade. They result from the self-assembly of surfactant molecules into long cylindrical aggregates that form a viscoelastic entangled network in the semidilute regime.

Under shear several experimental studies involving neutron scattering [9] and flow birefringence [10] support the picture of a localized alignment of wormlike micelles into a highly sheared band of low viscosity, that coexists with a weakly oriented, entangled solution of much higher viscosity (see Ref. [5] for a recent review). The rheological signature of shear banding is a very strongly shear-thinning behavior above some critical shear rate $\dot{\gamma}_1$, which shows up on the flow curve as a stress plateau at a well-defined shear stress $\sigma^\star$ between $\dot{\gamma}_1$ and a second critical shear rate $\dot{\gamma}_2 \gg \dot{\gamma}_1$. Increasing the applied shear rate $\dot{\gamma}$ induces the growth of the high-shear band of viscosity $\eta_2=\sigma^\star/\dot{\gamma}_2$ within the low-shear band of viscosity $\eta_1=\sigma^\star/\dot{\gamma}_1$. In the absence of wall slip, the continuity of the velocity across the interface between the bands leads to the so-called lever rule, that relates the proportion of each band to the shear rate $\dot{\gamma}=(1-\phi_2)\dot{\gamma}_1+\phi_2\dot{\gamma}_2$, where ϕ_2 is the proportion of the highly sheared material. The nucleation of a highly sheared band and its growth following the lever rule have been recently evidenced by local velocity measurements using dynamic light scattering [6] and particle tracking velocimetry [7] in the much studied cetylpyridinium chloride-sodium salicylate system in the semidilute regime [11].

Such a shear-banding scenario, hereafter referred to as the "classical shear-banding scenario," had been predicted theoretically by Cates and co-workers [12,13] through an extension of the Doi and Edwards model [14] including the breakage and the recombination processes typical of wormlike micelles. More recent theoretical approaches have helped to clarify the stress selection mechanisms along the stress plateau [15–18]. However, using a nuclear magnetic resonance (NMR) setup that allows one to record simultaneously the velocity field and the local structure of a sample under shear, Callaghan and co-workers have questioned the classical shear-banding scenario [19,20]. Indeed the data in Refs. [19,20], recorded in the cetyltrimethyl ammonium bromide (CTAB) in deuterated water (D_2O) system close to the thermodynamic isotropic-to-nematic (IN) transition, show the nucleation of an unsheared highly viscous region of nematic order in the stress plateau region instead of a low-viscosity aligned phase. This shear-induced structure was called a nematic gel by the authors. This study also pointed out the existence of temporal fluctuations of the flow field, which was confirmed later on using NMR in other concentrated micellar systems [21,22]. Unfortunately the local flow behavior of the sample could not be correlated to the rheological data since a metallic stress sensor cannot be placed into the NMR magnet. Finally birefringence experiments have also unveiled complex transients and temporal fluctuations incompatible with the classical, steady shear-banding scenario [23–25].

In a previous work [26] we reported significant progress in the development of time-resolved velocity measurements under shear: by applying a high-frequency ultrasonic velocimetry technique to the CTAB-D_2O system, we showed that, at a given position along the stress plateau and at a temperature of 44 °C, this particular micellar system undergoes both very slow relaxations (over ~6 h), which makes it hard to precisely define a steady state, and "fast" fluctuations (over ~50 s) correlated to wall slip dynamics. The present paper is devoted to a more comprehensive study of these "fast" dy-

*Present address: Polymères, Colloides, Interfaces, UMR CNRS, Université du Maine, 72085 Le Mans cedex 09, France. Lydiane.Becu@univ-lemans.fr
†Present address: Laboratoire de Physique, CNRS UMR 5672, École Normale Supérieure de Lyon, 46 allée d'Italie, 69364 Lyon cedex 07, France.
‡Present address: Rhodia Laboratoire du Futur, CNRS-FRE 2771, 178 Avenue Schweitzer, 33600 Pessac, France.

namics. We compare our results to those of Ref. [20] and find a perfect agreement between the two studies. Focusing on the fast dynamics of the flow and on apparent negative slip, we present an alternative explanation to the scenario proposed by Callaghan and co-workers. In particular our data set recorded at a temperature of 41 °C strongly suggests the presence of three-dimensional unsteady flows in the stress plateau region. Our study is completed by structural measurements using small angle x-ray scattering (SAXS) under shear.

The article is organized as follows. The experimental setups for ultrasonic velocimetry and SAXS measurements are described in Sec. II together with the micellar system under study. Section III presents experimental results obtained at a temperature $T=32$ °C, i.e., in the thermodynamic nematic phase of our sample. Section IV deals with the experiments performed in the isotropic phase at $T=41$ °C. Finally the discussion of Sec. V provides a comparison of our results to those of Ref. [20], addresses the possible origins of three-dimensional flow dynamics, and raises the question of the influence of wall slip on the bulk dynamics.

II. EXPERIMENTAL SECTION

A. Velocimetry setup

Our rheoultrasonic setup allows the recording of velocity profiles across the gap of a Couette cell simultaneously to rheological data. This setup has been described at length in Ref. [27] and only its main characteristics are recalled here. It is composed of a stress-controlled rheometer (TA Instruments AR1000N) equipped with a Couette cell made of Plexiglas (gap $e=1$ mm, inner radius $R_1=24$ mm, and height $H=30$ mm). The whole cell is surrounded by water whose temperature is kept constant to within ±0.1 °C. To prevent evaporation, the cell is closed by a PVC lid that rests on the stator. On the rotor side, the lid plunges into a small cylindrical water reservoir machined on the top part of the rotor, which both acts as a solvent trap and ensures watertightness. The rheometer imposes a constant torque Γ on the axis of the Couette cell which induces a stress σ in the fluid. The rotation speed Ω of the Couette cell from which the shear rate $\dot{\gamma}$ can be deduced is continuously recorded. A computer-controlled feedback loop on the applied torque Γ can be used to apply a constant shear rate without any significant temporal fluctuations ($\delta\dot{\gamma}/\dot{\gamma}\approx 0.01\%$).

Let us note σ and $\dot{\gamma}$ the shear stress and the shear rate indicated by the rheometer. The relationships between $(\sigma,\dot{\gamma})$ and (Γ,Ω) read

$$\sigma = \frac{R_1^2+R_2^2}{4\pi H R_1^2 R_2^2}\Gamma, \tag{1}$$

$$\dot{\gamma} = \frac{R_1^2+R_2^2}{R_2^2-R_1^2}\Omega. \tag{2}$$

Such definitions ensure that $(\sigma,\dot{\gamma})$ correspond to the average values of the local stress $\sigma(x)$ and shear rate $\dot{\gamma}(x)$ in the case of a Newtonian fluid (x denotes the radial position in the gap of the Couette cell). It is very important not to confuse the averaged quantities $(\sigma,\dot{\gamma})$, hereafter referred to as the engineering quantities, with the local quantities $[\sigma(x),\dot{\gamma}(x)]$. Moreover, the shear rate $\dot{\gamma}$ given by the rheometer may differ from the true shear rate $\dot{\gamma}_{\text{true}}$ in the sample due to the presence of wall slip or heterogeneous flows. In the following, the nature (engineering, local, or true) of the variables will be specified whenever confusion is possible.

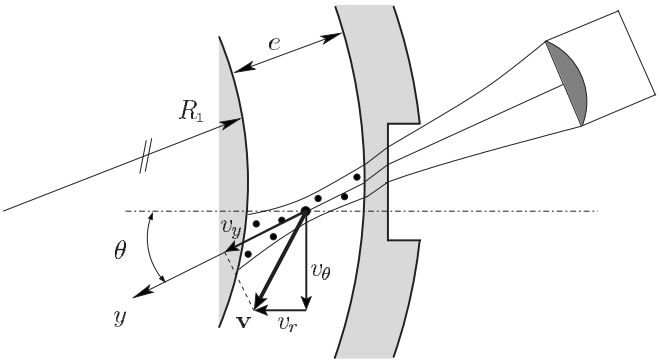

FIG. 1. Experimental setup for ultrasonic velocimetry under shear in a Couette geometry. The notations are defined in the text.

A piezopolymer transducer of central frequency $f=36$ MHz generating focused ultrasonic pulses is immersed in water in front of the stator as sketched in Fig. 1. A small rectangular window of minimal thickness 0.5 mm milled in the stator allows one to limit the attenuation of the ultrasonic signal due to Plexiglas. Once inside the fluid, ultrasonic pulses get scattered by small latex spheres suspended in the micellar system (see Sec. II C below). Ultrasonic echoes backscattered toward the transducer are sampled at 500 MHz, stored on a high-speed PCI digitizer (Acqiris DP235), and transferred to the host computer for postprocessing.

Under the assumption of single scattering, the signal received at time t can be interpreted as interferences coming from scatterers located at position $y=c_0t/2$, where c_0 is the sound speed in the fluid and y the distance from the transducer along the ultrasonic beam (see Fig. 1). When the sample is submitted to a shear flow, the backscattered signals move along with the scatterers. Two successive pulses separated by a time lag T lead to two similar backscattered signals that are shifted in time. One can relate the time shift $\delta t(t)$ between two echoes received at time t to the displacement of the scatterers $\delta y(y)=c_0\delta t(t)/2$ at position y. The velocity profile $v_y(y)$ (i.e., the y component of the velocity vector $\mathbf{v}$) is then simply given by $v_y(y)=\delta y(y)/T$. A cross-correlation algorithm is used to estimate the time shift δt as a function of t, and the sound speed c_0 is measured independently (see Ref. [27] for more details). In order to get a nonzero projection of the velocity along the acoustic axis, ultrasonic pulses enter the gap with an angle $\theta\simeq 15°$ as shown in Fig. 1. In addition, a careful choice of this angle allows one to minimize the reflections at the water-Plexiglas and Plexiglas-sample interfaces.

Using the notations of Fig. 1, the projection v_y of the velocity vector $\mathbf{v}$ along the y axis in Couette geometry is the sum of the projections of the radial component v_r and of the tangential component v_θ of $\mathbf{v}$:

$$v_y = v_\theta \sin\theta + v_r \cos\theta. \quad (3)$$

Assuming the flow field to be purely tangential (which remains valid as long as no hydrodynamic or elastic instability takes place nor any other three-dimensional flow), one gets

$$v_\theta(x) = \frac{v_y(y)}{\sin\theta} \equiv v(x), \quad (4)$$

where x is the radial position given by $x=e-y\cos\theta$. The determination of $v(x)$ thus requires a precise determination of the angle θ, which is achieved through a calibration procedure using a Newtonian fluid [27].

If the radial component v_r is nonzero, the term $v_r\cos\theta$ comes into play in Eq. (3), so that the definition of $v(x)$ given in Eq. (4) leads to

$$v(x) = v_\theta(x) + \frac{v_r(x)}{\tan\theta}. \quad (5)$$

Therefore the interpretation of the experimental velocity profiles $v(x)$ may become problematic whenever the flow is not purely tangential. Note that this is also the case for other techniques such as dynamic light scattering or NMR where only a projection of the velocity vector is measured. With our ultrasonic setup, $\tan\theta \simeq 0.25$ so that the second term in Eq. (5) actually amplifies the effect of the radial velocity by a factor of about 4. This sensitivity to v_r will help evidence three-dimensional flows in the micellar system under study. Finally, it should also be mentioned that our setup is insensitive to any contribution of the vertical component v_z of the velocity vector (i.e., in the vorticity direction z) since its projection along the acoustic axis is always zero.

To ensure a good statistical convergence, one velocity profile is obtained by averaging $v(x)$ over 50 series of 20 consecutive pulses. The spatial resolution of our experimental setup is of the order of 40 μm and the time needed to record one velocity profile ranges between 0.02 and 2 s depending on the applied shear rate [27].

B. SAXS setup

The SAXS measurements were performed on the high brilliance beamline *ID2* at the European Synchrotron Radiation Facility in Grenoble, France. The pinhole camera setup and the procedure for data acquisition and analysis are described elsewhere [28]. The beam size at the sample position was about 0.1×0.1 mm. Two-dimensional SAXS patterns are acquired using an image intensified charge-coupled detector. The incident wavelength was $\lambda=0.099$ nm and a sample-to-detector distance of 6 m was used. This combination provided a scattering wave vector $\mathbf{q}$ in the range $0.1 < q < 2$ nm^{-1}, where $q=\|\mathbf{q}\|=(4\pi/\lambda)\sin(\phi/2)$, ϕ being the scattering angle. The total acquisition time for a SAXS pattern was less than 1 s.

The sample was contained in a polycarbonate Searle-type Couette cell of gap $e=1$ mm and inner diameter $R_1=20$ mm coupled to a stress-controlled rheometer (Haake Roto-Visco RT20) [29]. An inner thermostated stage allows a temperature control around the cell to within 0.05 °C. Measurements are taken in radial configuration, i.e., with the beam passing along the velocity gradient direction through the center of the shear cell. The SAXS spectra thus encompass structural information over the whole width of the gap.

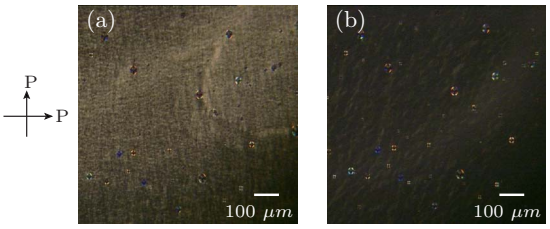

FIG. 2. (Color online) Optical microscopy pictures of the CTAB-D_2O wormlike micelle solution under crossed polarizers (P) at (a) $T=37$ °C and (b) $T=39$ °C. The IN transition occurs at $T=38$ °C. The Maltese crosses correspond to the latex spheres used to provide acoustic contrast (see text).

Although the differences in the velocimetry and SAXS setups (temperature control, cell geometry, rheological procedures) will not allow for a quantitative comparison of the rheological measurements, SAXS data under shear provide useful structural information that will help interpret the flow behavior.

C. System under study

We focus on a salt free wormlike micelle solution made of cetyltrimethyl ammonium bromide (CTAB) at 20 wt. % in deuterated water (D_2O) [19,20]. Since this solution is initially transparent to ultrasound, the system is seeded with 1 wt. % homemade latex spheres of diameter 5–10 μm in order to provide good acoustic contrast. This low quantity of scatterers allows us to obtain a measurable signal in the single scattering regime without significantly affecting the rheology of the sample. All the measurements presented here (including SAXS measurements) were performed in the presence of latex spheres.

When the temperature is decreased from the isotropic phase, a highly birefringent phase can be observed by optical microscopy under crossed polarizers which corresponds to the nematic ordered phase (see Fig. 2). Using a Mettler heating stage, we determined this IN transition to occur at 38 °C in our sample.

Rheological and velocimetry data were recorded at two distinct temperatures 32 and 41 °C while the SAXS experiments were performed at 30 and 41 °C. In the following we first present the results obtained in the nematic phase at $T=30$ and 32 °C. We then describe the experiments performed in the isotropic phase at $T=41$ °C. To conclude this experimental section, let us stress again that our velocimetry setup only measures the projection of the velocity profile on the y axis and does not provide a comprehensive image of a three-dimensional velocity field.

III. FLOW IN THE THERMODYNAMIC NEMATIC PHASE

A. Experimental procedure and rheological measurements

The sample, which was previously stored at 50 °C, is loaded in the thermostated Couette cell and half an hour is

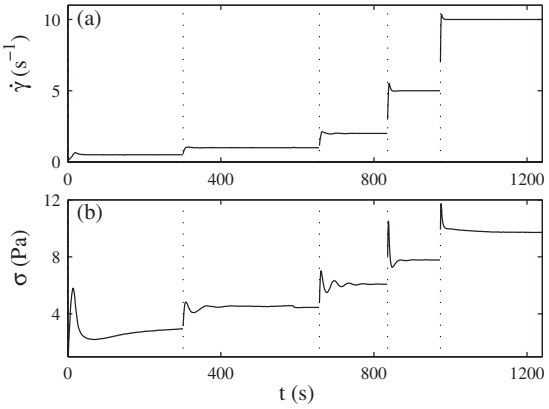

FIG. 3. Engineering rheological data recorded in the thermodynamic nematic phase at $T=32$ °C. (a) Imposed shear rate $\dot{\gamma}(t)$ for $\dot{\gamma}=0.5$, 1, 2, 5, and 10 s^{-1}. (b) Corresponding shear stress responses $\sigma(t)$. The dotted lines indicate the beginning of each step. Time $t=0$ corresponds to the beginning of the experiment when the smallest shear rate $\dot{\gamma}=0.5$ s^{-1} is applied.

allowed for temperature equilibration before starting the experiment. Engineering rheological data are then recorded every second simultaneously to velocity profiles. The rheological protocol consists in applying shear rate steps of duration comprised between 140 and 300 s and of values ranging from 0.5 to 1000 s^{-1}. The shear rate increment between two successive steps is chosen in order to provide a logarithmic sampling.

Examples of engineering rheological signals are displayed in Fig. 3. We check that the applied shear rate $\dot{\gamma}(t)$ does not present significant fluctuations after a short transient of a few seconds. For all the steps, the shear stress $\sigma(t)$ reaches a stationary value in less than 100 s. The transient regime is characterized by damped oscillations of $\sigma(t)$. This phenomenon has already been reported in other nematic systems and could be attributed to the nematic tumbling instability [30,31] or to a coupling between the elastic properties of the fluid and the inertia of the rheometer.

The engineering flow curve of Fig. 4 is obtained by averaging the stress response over the last 20 s of each step. It is well described by a power law $\sigma=A\dot{\gamma}^n$ with $A=3.9$ Pa s^n and $n=0.4$. According to engineering rheological measurements, the nematic phase of our wormlike micelle solution is thus shear thinning.

B. Velocity profiles

To describe the local flow behavior of the nematic phase, we record 5 to 15 individual velocity profiles in the stationary regime. The time interval between two successive measurements of individual profiles depends on the applied shear rate and is around 50 s at 0.5 s^{-1}, 8 s at 5 s^{-1}, and 2 s at 50 s^{-1} and above. Figure 5 presents velocity profiles averaged over all the profiles recorded for various applied shear rates. The error bars stand for the standard deviations of the velocity measurements and are of the order of the symbol size, which demonstrates that the flow is steady. These time-averaged velocity profiles are almost linear and do not present any shear bands, unlike the isotropic phase as will be shown below.

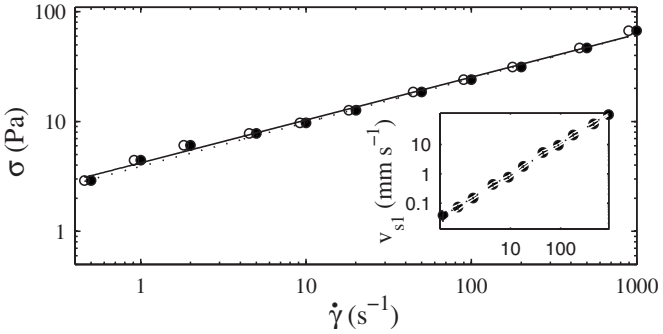

FIG. 4. Flow curve $\sigma(\dot{\gamma})$ at $T=32$ °C under controlled shear rate obtained by averaging the shear stress over the last 20 s of each step. The filled symbols (●) are the raw data and the open symbols (○) are data corrected from wall slip. The dotted and solid lines are the best fits with a power law $\sigma=A\dot{\gamma}^n$ of the raw data with $A=3.9$ Pa s^n and $n=0.4$ (dotted line) and of the data corrected from wall slip with $A=4.2$ Pa s^n and $n=0.39$ (solid line). Inset: slip velocity v_{s1} as a function of the true shear rate $\dot{\gamma}_{\text{true}}$. The dotted line is the best fit of v_{s1} vs $\dot{\gamma}_{\text{true}}$ with a power law of exponent 1.05.

However, it clearly appears that the velocity v_1 of the wormlike micelle solution in the vicinity of the inner cylinder never reaches the rotor velocity $v_0=R_1\Omega$ (indicated by arrows in Fig. 5), which reveals the occurrence of wall slip at the rotor. To quantify wall slip effects, we define the slip velocity at the rotor $v_{s1}=v_0-v_1$ as the difference between the rotor velocity v_0 and the fluid velocity close to the rotor $v_1=v(x\simeq 0)$. The slip velocity at the stator v_{s2} is simply given by the fluid velocity at the stator $v_2=v(x\simeq e)$. In practice, to estimate v_1 and v_2, a linear regression of the velocity profiles is performed over $0\leqslant x\leqslant 150$ μm and $e-150$ μm$\leqslant x\leqslant e$, respectively. The uncertainty on such a measurement is roughly ± 1 mm s^{-1}. As shown in the inset of Fig. 4, v_{s1}

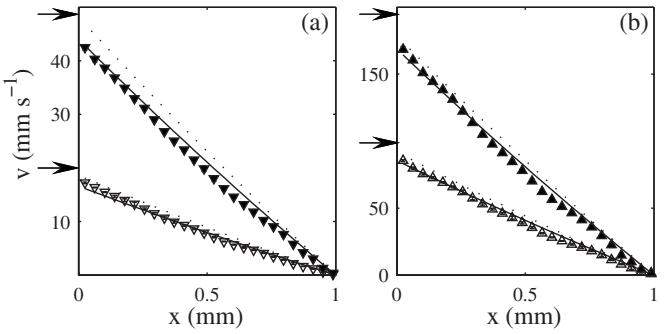

FIG. 5. Time-averaged velocity profiles $\langle v(x)\rangle$ recorded in the thermodynamic nematic phase at $T=32$ °C for (a) $\dot{\gamma}=20$ (▽), 50 (▼), (b) 100 (△), and 200 s^{-1} (▲). The standard deviation of these estimates are always smaller than the symbol size. Arrows indicate the rotor velocity v_0 at $\dot{\gamma}=20$, 50, 100, and 200 s^{-1}, respectively, $v_0=19.6$, 48.96, 97.9, and 195.8 mm s^{-1}. The dotted lines are the theoretical profiles calculated from the power-law fit of the engineering flow curve $\sigma=3.9\dot{\gamma}^{0.4}$ whereas the solid lines correspond to the power-law fit of the data corrected from wall slip $\sigma=4.2\dot{\gamma}^{0.39}$ (see text).

increases linearly with the applied shear rate $\dot{\gamma}$: one has $v_{s1} < 1$ mm s^{-1} for $\dot{\gamma} < 10$ s^{-1}, $v_{s1} = 5.4$ mm s^{-1} at $\dot{\gamma} = 50$ s^{-1}, and $v_{s1} = 103$ mm s^{-1} at $\dot{\gamma} = 1000$ s^{-1}. On the other hand v_{s2} never exceeds 1 mm s^{-1} and can be considered as negligible over the whole range of applied shear rates.

A consequence of wall slip is that the shear rate experienced by the solution is lower than the engineering shear rate $\dot{\gamma}$. We thus define a true shear rate $\dot{\gamma}_{\text{true}}$ by removing wall slip effects using

$$\dot{\gamma}_{\text{true}} = \frac{R_1^2 + R_2^2}{R_1(R_1 + R_2)} \frac{v_1 - v_2 \dfrac{R_1}{R_2}}{e}. \tag{6}$$

The first term in Eq. (6) allows one to take into account the stress inhomogeneity in the Couette cell and thus to get a quantitative comparison between the true shear rate $\dot{\gamma}_{\text{true}}$ and the engineering shear rate $\dot{\gamma}$ computed using Eq. (2). The true flow curve σ vs $\dot{\gamma}_{\text{true}}$ is superimposed to the engineering flow curve in Fig. 4. The true flow curve is also well described by a power law $\sigma = A\dot{\gamma}^n$ but with slightly different parameters $A = 4.2$ Pa s^n and $n = 0.39$.

Going further into the analysis of the experimental data, we show that a power-law behavior also accounts for the shape of our velocity profiles. Indeed assuming the local rheological behavior $\sigma(x) = A\dot{\gamma}(x)^n$ and defining the local rheological variables by

$$\sigma(x) = \frac{\Gamma}{2\pi H r^2} \quad \text{and} \quad \dot{\gamma}(x) = -r\frac{\partial}{\partial x}\frac{v(x)}{r}, \tag{7}$$

where $r = R_1 + x$ and Γ is the torque applied on the rotor axis, the velocity profile is easily calculated by integration with the boundary condition $v(x = e) = 0$ and reads

$$v(x) = r\frac{n}{2}\left[\frac{\Gamma}{2\pi H R_2^2 A}\right]^{1/n}\left[\left(\frac{R_2}{r}\right)^{2/n} - 1\right]. \tag{8}$$

The solid lines in Fig. 5 are the velocity profiles given by Eq. (8) and calculated for the parameters deduced from the true flow curve: $A = 4.2$ Pa s^n and $n = 0.39$. These theoretical velocity profiles fit the whole experimental data set very satisfactorily. The local velocity measurements are thus in good agreement with the global rheological measurement corrected from wall slip. Theoretical velocity profiles calculated for the parameters $A = 3.9$ Pa s^n and $n = 0.4$ deduced from the engineering flow curve are also shown as dotted lines in Fig. 5. They fail in describing all the velocity profiles, which illustrates the sensitivity of the local quantities to slight changes in the global parameters and stresses the fact that wall slip can lead to significant errors on the rheological law derived from engineering values [32].

C. SAXS measurements

The above results show that the thermodynamic nematic phase of the CTAB-D_2O system behaves as a slightly shear-thinning fluid and that the flow remains homogeneous as the shear rate is varied. A weakly shear-thinning behavior may be related to the coupling between the flow and the structure of the nematic phase. This is indeed confirmed by SAXS measurements under shear. Figure 6 shows the SAXS patterns recorded in our sample at 30 °C at rest [Fig. 6(a)] and under shear at $\dot{\gamma} = 300$ s^{-1} [Fig. 6(b)]. The wave vectors $\mathbf{q}_\omega$ and $\mathbf{q}_v$ correspond to the directions of vorticity and velocity in direct space, respectively.

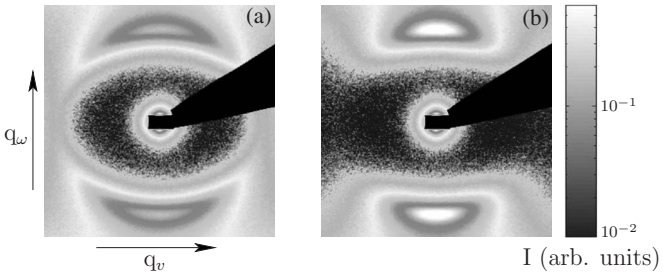

FIG. 6. Two-dimensional SAXS patterns recorded in the thermodynamic nematic phase at $T = 30$ °C for (a) $\dot{\gamma} = 0$ s^{-1} after preshearing and (b) $\dot{\gamma} = 300$ s^{-1}. The scattered intensity is recorded along the reciprocal axes $(\mathbf{q}_v, \mathbf{q}_\omega)$ for $\|\mathbf{q}\|$ ranging from 0 to 2 nm^{-1}.

The spectra are characterized by crescentlike peaks in the $\mathbf{q}_\omega$ direction which are related to alignment of the micelles in the velocity direction [33]. At rest and under shear, the intensity maximum is found at $\|\mathbf{q}\| = \|\mathbf{q}_{\max}\| = 0.82$ nm^{-1}. The mean distance between the center of mass of the micelles, which is not affected by the flow, can be roughly estimated as $2\pi/\|\mathbf{q}_{\max}\| = 7.65$ nm. Since the width of these peaks is linked to the distribution of the nematic director, the refinement of the peaks observed at $\dot{\gamma} = 300$ s^{-1} points to an increase of the nematic orientational order under flow. Such a result has already been reported in the thermodynamic nematic phase of another concentrated system of wormlike micelles made of cetylpyridinium chloride and hexanol in brine [34].

IV. FLOW IN THE ISOTROPIC PHASE AT $T = 41$ °C

A. Experimental procedure and rheological measurements

After temperature equilibration, we apply shear rate steps from 0.1 to 400 s^{-1} with a logarithmic sampling. The duration of the steps is 900 s except for $\dot{\gamma} = 40$ and 70 s^{-1} which have been extended to 2700 and 1800 s in order to capture the flow dynamics.

Typical engineering rheological signals are shown in Fig. 7. We check that the rheometer applies a constant shear rate: here the amplitude of the fluctuations $\delta\dot{\gamma}/\dot{\gamma}$ never exceeds 0.5%. At all shear rates, the short-time shear stress response $\sigma(t)$ is characterized by an overshoot due to the elastic behavior of the sample [35]. For $\dot{\gamma} \leqslant \dot{\gamma}_1 \simeq 10$ s^{-1}, the system then reaches a stationary state in less than 100 s. For $\dot{\gamma}_1 < \dot{\gamma} < \dot{\gamma}_2 \simeq 200$ s^{-1}, the characteristic time for stress relaxation becomes very long and we can not ascertain that the system has reached steady state even after 2700 s. Such very slow dynamics in the plateau region have already been reported in this system [10,26]. In particular our previous study performed at $T = 44°$ revealed that it could take several hours for the shear stress to reach a stationary value [26]. Moreover along the stress plateau the shear stress response shows no-

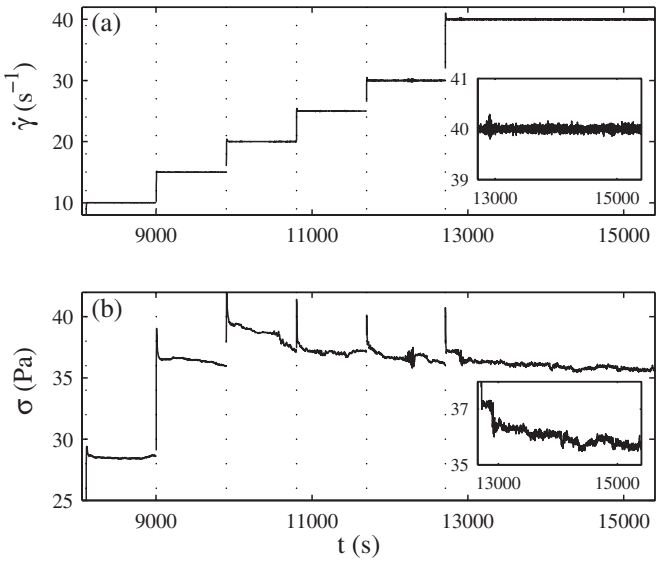

FIG. 7. Engineering rheological data recorded in the isotropic phase at $T=41$ °C. (a) Imposed shear rate $\dot{\gamma}(t)$ in the stress plateau at $\dot{\gamma}=10$, 15, 20, 25, 30, and 40 s^{-1}. Inset: enlargement of $\dot{\gamma}(t)$ for $\dot{\gamma}=40$ s^{-1}. (b) Corresponding shear stress responses $\sigma(t)$. Inset: enlargement of $\sigma(t)$ for $\dot{\gamma}=40$ s^{-1}. The dotted lines indicate the beginning of each step. Time $t=0$ corresponds to the beginning of the experiment when the smallest shear rate $\dot{\gamma}=0.5$ s^{-1} is applied.

ticeable fluctuations of amplitude $\delta\sigma/\sigma \simeq 1.5\%$ as can be seen in the inset of Fig. 7.

The engineering flow curve obtained by averaging the shear stress response over the last 100 s of each step is plotted in Fig. 8. It reveals a stress plateau at $\sigma^{\star}=36.5\pm0.7$ Pa that extends from $\dot{\gamma}_1 \simeq 10$ s^{-1} to $\dot{\gamma}_2 \simeq 200$ s^{-1}, a feature typical of shear-banded flows as recalled in the Introduction. Let us note, however, that due to the very slow dynamics described above, the rheological data in the plateau region do not correspond to stationary states.

B. Time-averaged velocity profiles

Figure 9 presents the velocity profiles averaged over the last 100 s of each rheological step. Since the interval between two successive measurements of individual profiles was 3 s, the data of Fig. 9 are averaged over approximately

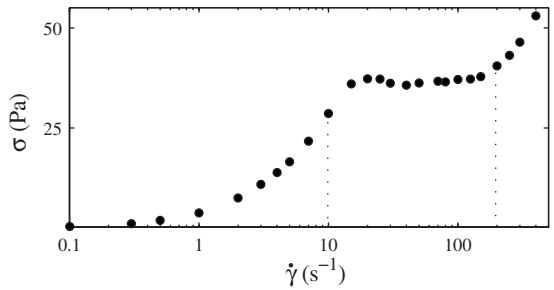

FIG. 8. Engineering flow curve $\sigma(\dot{\gamma})$ at $T=41$ °C under controlled shear rate obtained by averaging the shear stress over the last 100 s of each step. The dotted lines indicate the limits of the stress plateau $\dot{\gamma}_1 \simeq 10$ s^{-1} and $\dot{\gamma}_2 \simeq 200$ s^{-1}.

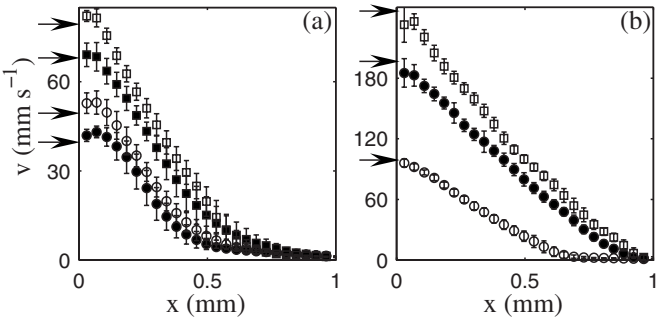

FIG. 9. Time-averaged velocity profiles $\langle v(x)\rangle$ recorded in the isotropic phase at $T=41$ °C for (a) $\dot{\gamma}=40$ (●), 50 (○), 70 (■), 80 s^{-1} (□) and (b) $\dot{\gamma}=100$ (○), 200 (●), and 250 s^{-1} (□). The error bars are the standard deviations of these estimates. Arrows indicate the rotor velocities.

30 profiles. The error bars correspond to the standard deviations, which are significantly larger than those previously reported in the thermodynamic nematic phase (see Sec. III B), pointing out the occurrence of strong temporal fluctuations of the flow field. The local flow behavior along the stress plateau is characterized by the coexistence of bands bearing different shear rates. As the engineering shear rate is increased, the high-shear band grows and progressively fills the gap, which at first sight seems compatible with the classical shear-banding scenario. Note that, at this temperature, no significant wall slip is detected. However, a careful inspection of the time-averaged velocity profiles of Fig. 9(a) reveals the existence of a small unsheared region of width 100 μm close to the rotor, in which the fluid velocity is slightly larger than the rotor velocity v_0. This region is strongly reminiscent of the highly viscous, nematic gel pointed out by Fischer and Callaghan using NMR velocimetry [19,20]. A more detailed description of this phenomenon is given in the next section.

Moreover, the rheological signals of Fig. 7 suggest that the system has not reached steady state at the end of each step. Very long equilibration times have already been reported in the study of Ref. [26] performed on the same system. As a consequence, the velocity profiles of Fig. 9 cannot be interpreted in terms of the classical shear-banding scenario which applies to stationary states. In particular the growth of the highly sheared band cannot be described by the lever rule with the shear rates $\dot{\gamma}_1$ and $\dot{\gamma}_2$ inferred from the flow curve. A clear indication that this scenario cannot be invoked to analyze the present experiments is the strong increase of the local shear rate in the highly sheared band from $\dot{\gamma}_2 \simeq 120$ to 300 s^{-1} as the engineering shear rate is increased (compare, for instance, the velocity profiles at 70 and 80 s^{-1} for which the position of the interface between the two shear bands is almost constant while $\dot{\gamma}_2$ noticeably increases). This observation does not necessarily mean that the classical shear-banding scenario does not hold for the present system in its asymptotic state. Indeed experiments performed at 44 °C over 6 h have shown that the final position of the interface was consistent with the lever rule [26]. Therefore no definite conclusion can be drawn from the present data since they were recorded over 15 to 45 min per step.

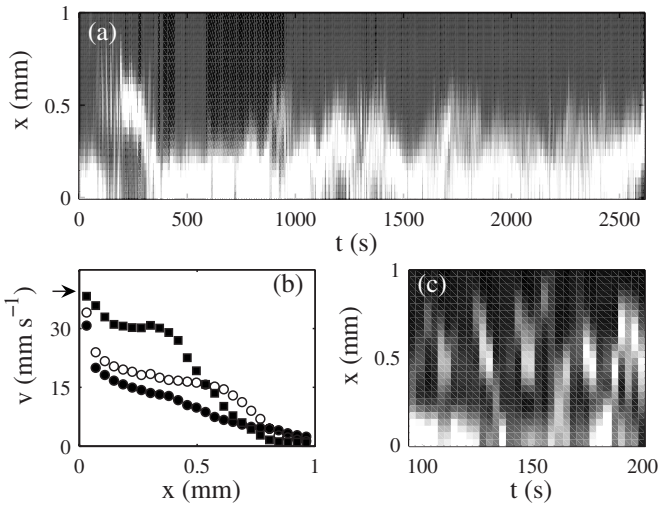

FIG. 10. Description of the flow dynamics at $\dot{\gamma}=40\ s^{-1}$ for $T=41\ °C$. (a) Local shear rate $\dot{\gamma}(x,t)$. A linear gray scale is used: black and white correspond, respectively, to $\dot{\gamma}=0\ s^{-1}$ and $\dot{\gamma}\geqslant 100\ s^{-1}$. (b) Velocity profiles during the apparition of an unsheared region at $t=138$ (●), 142 (○), and 145 s (■). (c) Enlargement of $\dot{\gamma}(x,t)$ over $t=95$–200 s. The rotor velocity is $v_0=39.9\ mms^{-1}$ and is indicated by an arrow in (b).

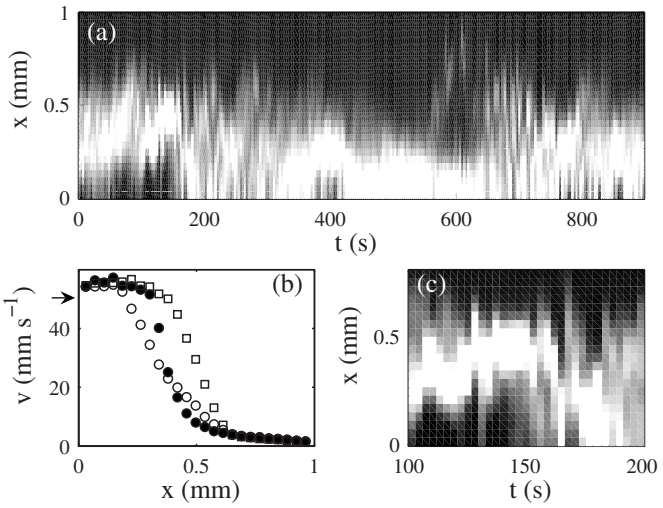

FIG. 11. Description of the flow dynamics at $\dot{\gamma}=50\ s^{-1}$ for $T=41\ °C$. (a) Local shear rate $\dot{\gamma}(x,t)$. A linear gray scale is used: black and white correspond, respectively, to $\dot{\gamma}=0\ s^{-1}$ and $\dot{\gamma}\geqslant 120\ s^{-1}$. (b) Velocity profiles at $t=118$ (○), 124 (●), and 127 s (□). (c) Enlargement of $\dot{\gamma}(x,t)$ over $t=100$–200 s. The rotor velocity is $v_0=49.9\ mm\ s^{-1}$ and is indicated by an arrow in (b).

C. Description of the flow dynamics

In this paragraph we focus on the data recorded at $\dot{\gamma}=40$ and $50\ s^{-1}$ which illustrate the various features of the flow dynamics in the shear banding regime. The phenomena described below are generic of the flow behavior along the stress plateau.

1. Step at $\dot{\gamma}=40\ s^{-1}$

In order to highlight the flow dynamics, the local shear rate $\dot{\gamma}(x,t)$ is estimated by differentiating the velocity profiles $v(x,t)$ according to

$$\dot{\gamma}(x,t) = -(R_1+x)\frac{\partial}{\partial x}\frac{v(x,t)}{R_1+x}. \tag{9}$$

Since such a spatial derivative is very sensitive to the experimental uncertainty, the local shear rates are averaged over three consecutive positions centered around x. For each mean position x and each time t, $\dot{\gamma}(x,t)$ is coded in linear gray levels, the darker value corresponding to smaller shear rates, and presented as a function of time t (abscissae) and position x (ordinates) in the spatiotemporal diagram of Fig. 10(a). Such a representation clearly shows that the flow is inhomogeneous and unsteady. Consistently with the averaged profiles of Fig. 9, a high-shear band located in the vicinity of the rotor (white region near $x=0$) coexists with a low-shear band located near the stator (black region near $x=e$).

The fluctuations of the flow can be described by two different mechanisms. (i) Strong fluctuations of the position of the interface between the two shear bands from $x\simeq 0.3$ mm to $x\simeq 0.5$ mm, with a time scale ranging from 3 to 200 s. These fluctuations are similar to those already described in Ref. [26]. (ii) The intermittent apparition of weakly sheared zones close to the inner cylinder. These events, unseen in previous experiments on the same system at a higher temperature [26], appear as black patches for $x<0.5$ mm in the spatiotemporal diagram for $t=100$–300 s, $t=1100$–1300 s, and $t=2500$–2620 s.

In order to better describe one of the intermittent events mentioned in point (ii) above, Fig. 10(b) presents three individual velocity profiles recorded for $t=100$–200 s. The velocity field is initially divided into two shear bands (● symbols). An unsheared zone then suddenly appear for $x=0.1$–0.5 mm (○ and ■ symbols). This zone intermittently disappears, as revealed by the enlargement of the spatiotemporal diagram over $t=95$–200 s shown in Fig. 10(c) (see the alternatively black and white regions), suggesting dynamics faster than our temporal resolution of 3 s. Highly unstable transient profiles bearing at least three different shear bands are recorded during this process. Their nucleation is associated to fast and large amplitude fluctuations of the velocity field: in Fig. 10(b), the local velocity $v(x,t)$ at $x\simeq 0.4$ mm increases from 10 to 30 mms^{-1} in 7 s. Finally, the unsheared band moves towards the rotor and remains stable for more than 100 s [see the black patch for $x\leqslant 0.4$ mm and $t=200$–300 s in Fig. 10(a)].

2. Step at $\dot{\gamma}=50\ s^{-1}$

The dynamics of the flow for $\dot{\gamma}=50\ s^{-1}$ are summarized in Fig. 11. The spatiotemporal diagram of Fig. 11(a) again reveals large fluctuations of the position of the interface between the two shear bands from $x\simeq 0.3$ to $x\simeq 0.5$ mm. Moreover, an unsheared zone is again evidenced near the inner cylinder (see the black region for $x\leqslant 0.4$ mm and $t=0$–160 s). However, contrary to the step at $\dot{\gamma}=40\ s^{-1}$, this zone appears in the vicinity of the rotor from the beginning of the experiment. From $t=0$ to $t=160$ s, the unsheared band widens from 200 μm to 400 μm [see Figs. 11(b) and 11(c)]

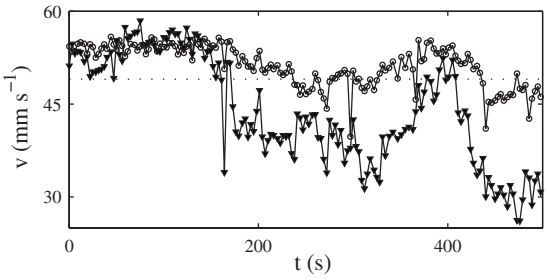

FIG. 12. Temporal evolution of the velocity $v(x_0,t)$ recorded at (a) $x_0=0$ mm (○) and (b) $x_0=0.15$ mm (▼) for $\dot{\gamma}=50$ s^{-1} and $T=41$ °C. The dotted line indicates the wall velocity v_0.

before disappearing. Such an unsheared region nucleates again intermittently around $t=400$ s and for $t>650$ s.

A careful inspection of the velocity profiles reveals an even more striking point. Figure 11(b) indeed shows that the local velocity in the unsheared band passes through a maximum for $x\simeq 0.1$–0.2 mm and that the maximum velocity is larger than the rotor velocity (indicated by an arrow on the figure). This local rise of the velocity with respect to the position in the gap leads to a slope of at least 26 rad/s, and thus cannot be accounted for by a rigid body rotation which would lead to a rate of increase of the order of 2 rad/s.

This last observation is clearly evidenced in Fig. 12, which presents the velocity signals recorded at positions $x_0=0$ mm and $x_0=0.15$ mm for $t<500$ s. Note that, although not commented by the authors, such subtle effects are also visible in Figs. 10 and 11 of Ref. [20]. In our experiments this phenomenon remains noticeable for more than 200 s: it cannot be understood in the framework of a purely orthoradial, axisymmetric flow, and such a result strongly suggests the occurrence of a three-dimensional instability.

Indeed, as already mentioned in Sec. II A, the existence of a nonzero radial component in the flow field leads to an additional contribution $v_r/\tan\theta$ to the experimental measurement v. Depending on v_r and θ, this additional term may contribute significantly to the velocity estimation v and induce the detection of velocities larger than v_0. In particular, since $\theta\simeq 10$–$15°$, one has $1/\tan\theta\simeq 3.7$–5.4 so that even a small value of the radial component v_r leads to a non negligible additional term. The simultaneous recording of two components of the velocity field could allow for a direct evidence of the occurrence of a three-dimensional flow, and is left for future work. It should also be added that this effect is likely to hide slip effects at the wall. Thus no definite conclusion about wall slip can be drawn at this temperature.

Finally the existence of a three-dimensional flow is confirmed by visual inspection of the fluid under shear: small air bubbles trapped in the micellar network show complicated three-dimensional trajectories and on very long time scales, the latex spheres seeding the flow tend to migrate and form unsteady, irregular patterns in the vorticity direction. Note that a three-dimensional instability of the interface between shear bands was also reported very recently in the cetyltrimethylammonium bromide and sodium nitrate system [36].

V. DISCUSSION

A. Summary and comparison with Fischer and Callaghan [20]

In Ref. [20], Fischer and Callaghan used NMR velocimetry to explore the local flow behavior of a concentrated CTAB-D_2O wormlike micelles solution in the isotropic phase close to the thermodynamic isotropic-to-nematic (IN) transition. With their setup, which has the crucial advantage of recording simultaneously velocity profiles and local structural information, the author detected an unsheared region of nematic order in the vicinity of the rotor. Moreover, they pointed out for the first time the existence of temporal fluctuations of the flow. In the following, we recall the main results gathered in the present work. Although our observations confirmed those of Ref. [20], our interpretation for these results differs from the one proposed by Fischer and Callaghan.

In Sec. III, it was clearly shown that the thermodynamic nematic phase of the CTAB-D_2O system flows and behaves as a standard shear-thinning fluid. The shear-thinning behavior can be explained by the increase of the orientational order under flow, a picture that is confirmed by SAXS measurements. We can therefore conclude that the flow behavior of the thermodynamic nematic phase thoroughly differs from that of the high-viscosity "gel" of nematic order revealed by rheo-NMR in Ref. [20].

In the isotropic phase, the flow curve is characterized by a stress plateau. When entering the plateau region, the shear stress relaxation becomes very slow and velocity measurements show that two bands of different viscosities coexist in the gap of the Couette cell. In the present experiments, the existence of very slow transients precludes any analysis of the velocity profiles in terms of the classical, stationary shear-banding scenario. We rather focused on the flow dynamics on "short" time scales ranging from 1 s to 15 min. Our velocity profile measurements revealed temporal fluctuations of two different kinds.

(i) Oscillations of the position of the interface between the two shear bands, which are correlated to the dynamics of the slip velocities, when detected.

(ii) The transient apparition of an unsheared region near the rotor, qualitatively similar to the one evidenced by Fischer and Callaghan [20]. However, although further developments of the NMR setup now allow for time-resolved measurements [37], the velocity profiles shown in Ref. [20] were averaged over 1 h and the fluctuations of the flow were only detected through the broadening of velocity distributions in NMR spectra.

Since the velocity in this region passes through a maximum and reaches values higher than the rotor velocity, we interpreted this phenomenon as the signature of a three-dimensional flow rather than of a "nematic gel." We stress the fact that this significant increase of the velocity with respect to the position in the gap cannot be accounted for by a solid-body rotation.

To further illustrate this last point, Fig. 13 presents velocity profiles recorded at 41 °C and averaged over specific time intervals, so that an apparently unsheared region is clearly visible for $x<0.2$ mm. These profiles should be com-

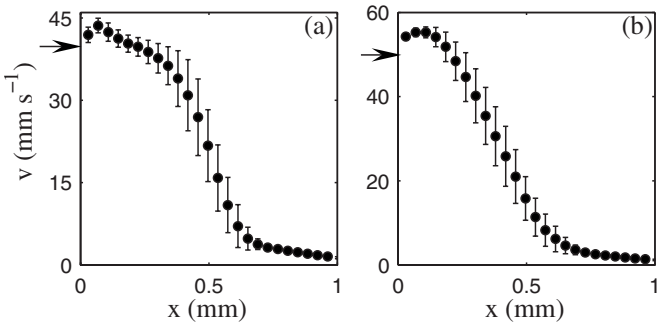

FIG. 13. Velocity profiles $\langle v(x) \rangle$ recorded in the isotropic phase at $T=41$ °C (a) for $\dot{\gamma}=40$ s^{-1} and averaged over $t=200$–300 s and (b) for $\dot{\gamma}=50$ s^{-1} and averaged over $t=10$–150 s. The error bars are the standard deviations of these estimates. Arrows indicate the rotor velocities.

pared to those of Figs. 10–12 from Ref. [20] obtained over an acquisition time of around 1 h. Our conclusion is that long averaging times may hide some strong spatiotemporal dynamics and that a three-dimensional instability of the flow (at least in the shear-induced phase close to the rotor) provides an alternative explanation for the peculiar velocity profiles of Fig. 13 which does not require to invoke the nucleation of a shear-induced "gel." However neither our ultrasound velocimetry setup not the NMR setup of Ref. [20] can, in their current versions, access simultaneously two different components of the velocity field.

B. Concentration fluctuations as a source for interface dynamics?

In the following, we discuss the possible cause for the instability of the interface between the shear bands observed experimentally. Previous studies have shown that a coupling between the flow and localized concentration fluctuations in the bands can induce the displacement of the interface [18]. In order to test this scenario, SAXS data were recorded under shear in the isotropic phase at $T=41$ °C. Figure 14 shows two typical SAXS patterns obtained below the stress plateau and within the stress plateau. Below the stress plateau [Fig. 14(a)], a ringlike spectrum is recorded, characteristic of an isotropic structure. At higher shear rates and within the stress plateau, two crescentlike peaks similar to those observed in the thermodynamic nematic phase (see Fig. 6) superimpose to the isotropic ring in the $\mathbf{q}_\omega$ direction. Such a pattern demonstrates the coexistence between an isotropic phase and a structure of nematic order in our sample sheared in the plateau region.

Moreover, as seen in Fig. 14(c), the diffracted intensity below the stress plateau is independent of the azimuthal angle ψ (defined as the angle between $\mathbf{q}$ and $\mathbf{q}_\omega$) and passes through a maximum for $\|\mathbf{q}\|=\|\mathbf{q}_{\max}\|=0.85$ nm^{-1}. The characteristic distance between the center of mass of the micelles can thus be estimated as $2\pi/\|\mathbf{q}_{\max}\| \simeq 7.4$ nm. Along the stress plateau [Fig. 14(b)], the scattered intensity is noticeably larger in the interval $-40° < \psi < 40°$ corresponding to the position of the peaks on the spectrum. Still, the maxima of intensities over both intervals of ψ are obtained for the same value $\|\mathbf{q}\|=\|\mathbf{q}_{\max}\|=0.85$ nm^{-1} which also exactly corresponds to the intensity maximum found at lower shear rates, i.e., in the isotropic phase.

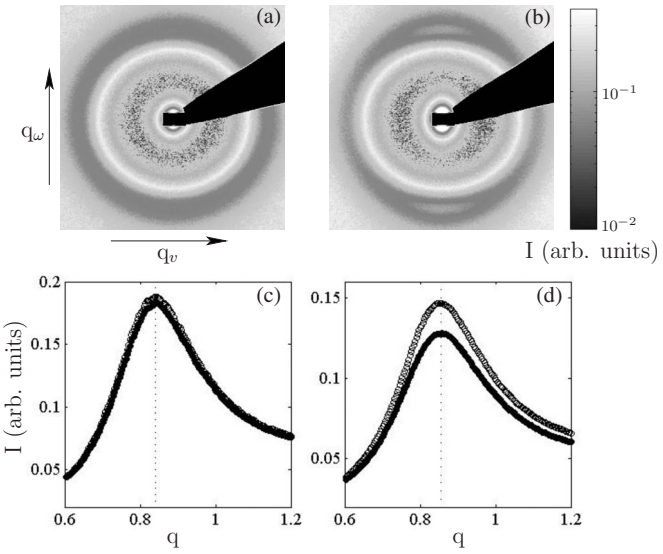

FIG. 14. Two-dimensional SAXS patterns recorded in the isotropic phase at $T=41$ °C (a) below the stress plateau and (b) in the stress plateau. The scattered intensity is recorded along the $(\mathbf{q}_v, \mathbf{q}_\omega)$ reciprocal axis for $\|\mathbf{q}\|=0$–2 nm^{-1}. The flow velocity is in real space parallel to $\mathbf{q}_v$. (c) and (d) are the integrated intensity along the azimuthal angle intervals $\psi=-40$–40° (open symbols) and $\psi=50$–130° (filled symbols).

These SAXS measurements allow us to conclude that the distance between the center of mass of the micelles remains unchanged in the shear-induced region of nematic order, which indicates that the separation of the flow into bands of different structures is *not* correlated to a local modification of the concentration in this system. Finally it should be noted that the mean distances between the micelles in the shear-induced phase and in the thermodynamic nematic phase are slightly different (7.4 nm here vs 7.65 nm in the thermodynamic nematic phase). This can be attributed to the difference in temperature. As a consequence, the present study does not allow any quantitative comparison between the structure of the shear-induced aligned band and the thermodynamic nematic phase but it allows us to rule out the existence of concentration differences between the two coexisting structures as a mechanism for interface fluctuations.

C. Possible origin for three-dimensional flows

Let us now review the various instabilities that are likely to lead to a three-dimensional flow in our sample.

(a) Taylor-Couette instability. It is well known that inertial instabilities such as the Taylor-Couette instability may occur at high rotation speeds of the inner cylinder [38]. In the case of a Couette flow, such instabilities are controlled by the Taylor number $\mathrm{Ta}=\rho^2\dot{\gamma}^2 e^5/\eta^2 R_1$, with ρ and η the density and the viscosity of the sample. In the experiments presented here, typical values of the parameters $e=1$ mm, $\dot{\gamma}=100$ s^{-1}, $R_1=24$ mm, $\eta=0.1$ Pa s, $\rho=1000$ kg m^{-3} lead to $\mathrm{Ta} \simeq 0.04$. Although the threshold value for the Taylor-

Couette instability in a complex fluid may differ from the critical value $Ta_c=1712$ for a Newtonian fluid, such a small value of Ta ensures that the flow can be considered as inertialess and allows us to rule out any inertial instability as a cause for a three-dimensional flow.

(b) Interface instability between two sheared fluids. In our experiments instability is observed in a two-phase region where a highly sheared phase coexists with weakly sheared micelles. Charru and co-workers [39] have shown that the interface between two immiscible fluids of different viscosities may be unstable when sheared in a Couette cell. The physical mechanism for this short-wavelength instability has been given by Hinch [40]: at the perturbed interface, the base flow velocities are discontinuous due to the viscosity contrast, and velocity disturbances must develop to satisfy continuity. The resulting vorticity disturbances are in phase with the deformed interface, but small out-of-phase components arise from advection by the base flow. The flow induced by these out-of-phase vorticity disturbances is such that the initial perturbation of the interface is amplified, at least for equal densities, leading to instability. Since this mechanism does not involve surface tension, it may also be applicable to two miscible fluids such as two micellar phases along the stress plateau.

Note, however, that in our case two time scales have to be compared: to allow the instability to develop, the time scale for the growth of the instability has to be shorter than that involved in the production of the shear-induced structure. Indeed, when the highly sheared phase bears a lower shear rate due to the perturbed flow, its structure tends to self-adapt to the new shear rate. The highly sheared phase may thus go back to the weakly sheared state. This may induce a displacement of the interface and a stabilization of the flow. Further investigation about the relevance of this two-fluid instability for shear-banded flows should focus on this time scale issue.

Moreover such an instability driven by the viscosity contrast between two fluids should disappear in the homogeneous regions, i.e., at very low or at very high shear rates when the low-shear or the high-shear phase fill the whole gap. The flow field at low shear rate is indeed laminar, and no experiment performed in the highly sheared region could clearly demonstrate that the flow remains unstable in this single-phase region. The development of the instability reported in Ref. [39] in our sample is thus compatible with our observations.

(c) Elastic instability. The viscoelasticity of the fluid may also induce an elastic instability in our sample, which shows up near the threshold as stationary roll cells [41–43]. This instability is driven by the same force which causes rod climbing of a highly elastic polymer fluid [44]: due to the cylindrical geometry, the motion of the complex fluid structure along a streamline may become unstable with respect to radial perturbations. Indeed radial perturbations induce a stretching of the structure of the complex fluid and a negative normal stress difference N_1. In cylindrical geometry this leads to a volume force N_1/R, where R is the radius of curvature, acting inwards in the radial direction. This force causes the increase of the radial perturbation. Such an elastic instability is seen when $(e/R_2)^{1/2}\mathrm{Wi}>M_c$, where e is the gap width, R_2 the external radius of the Couette cell, Wi the Weissenberg number defined as the ratio of the first normal stress difference N_1 to the shear stress σ, and M_c some critical number of order of magnitude 1 [45–47]. Note that the exact constant M_c corresponding to the instability threshold depends upon the constitutive model assumed for the fluid. One finds $M_c=5.92\pm0.02$ for both the upper-convected Maxwell model [42] and the Oldroyd-B model [14] when the shear viscosity of the solvent is half that of the sample [46].

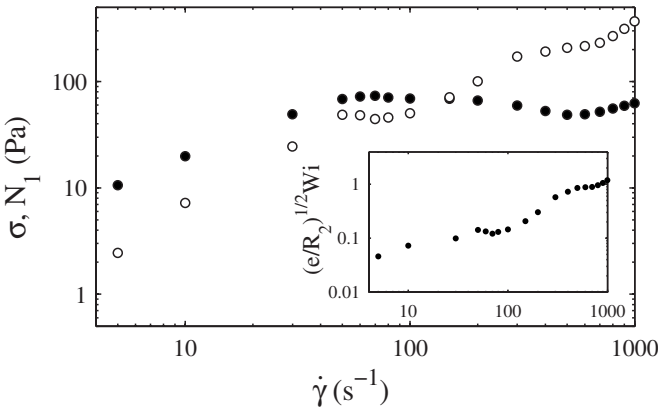

FIG. 15. Shear stress σ (●) and first normal stress difference N_1 (○) as a function of the imposed engineering shear rate $\dot{\gamma}$ recorded in cone-and-plate geometry at $T=41$ °C. The data were averaged over the last 100 s of each shear rate step of duration 300 s for $\dot{\gamma}<50$ s^{-1} and 900 s for $\dot{\gamma}\geqslant 50$ s^{-1}. Inset: $(e/R_2)^{1/2}\mathrm{Wi}$ as a function of the engineering shear rate $\dot{\gamma}$. Wi is the Weissenberg number defined as $\mathrm{Wi}=N_1/\sigma$.

Figure 15 presents the measurements of the shear stress σ and of the first normal stress difference N_1 as a function of the imposed engineering shear rate recorded in cone-and-plate geometry at $T=41$ °C. From these data, we can compute the Weissenberg number and test the criterion for elastic instability. As shown in the inset of Fig. 15, $(e/R_2)^{1/2}\mathrm{Wi}$ becomes of order 1 only on the high-shear branch of the flow curve (engineering shear rates $\dot{\gamma}>300$ s^{-1}). This value is less than $M_c=5.9$ predicted in the case of the Oldroyd-B and upper-convected Maxwell models. However we note that the above models considered so far in the theoretical analyses of the elastic instability [42,46] do not capture shear-thinning effects. Thus $(e/R_2)^{1/2}\mathrm{Wi}\simeq 1$ may be sufficient to trigger an elastic instability in our fluid along the high shear branch. In the plateau region, the instability criterion is more difficult to compute since two structures coexist. At first sight the global criterion computed from the engineering data remains of the order of 0.1. However, if a local Weissenberg number is estimated in the highly sheared phase and if a local criterion is applied with e being the width of the highly sheared band, values of order 0.5–1 are found, which may be sufficient to induce the instability. Our conclusion is that an elastic instability is a possible cause for the spatiotemporal dynamics and for the three-dimensional structure of the flow field observed in our CTAB-D_2O micellar system.

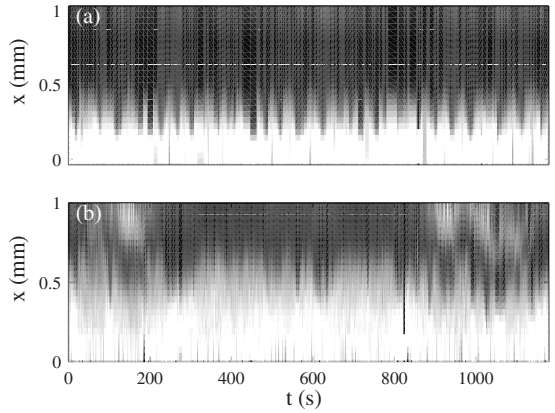

FIG. 16. Local shear rate $\dot{\gamma}(x,t)$ recorded at $\dot{\gamma}=400\ s^{-1}$ for $T=44\ °C$ (a) in a smooth Couette cell and (b) in a rough Couette cell. The same linear gray scale is used in both cases: black and white correspond, respectively, to $\dot{\gamma}=0\ s^{-1}$ and $\dot{\gamma}\geqslant 700\ s^{-1}$.

D. Perspectives

The present results still raise a number of open questions that should be addressed in order to fully understand the flow properties of the investigated micellar system. First more experimental effort will be devoted to the measurement of the flow behavior, which should help to firmly identify the origin of the three-dimensional features unveiled in the present data. Two-dimensional ultrasonic speckle imaging will provide us with simultaneous time-resolved recordings of the velocity profiles at different heights in the Couette cell by using a linear transducer array [48]. The relatively lower working frequencies of transducer arrays (typically 10 MHz vs 36 MHz in the present setup) will require larger gaps of 3–5 mm to compensate for the poorer spatial resolution. Moreover, since the curvature of the streamlines in the Taylor-Couette flow is likely to trigger three-dimensional unstable flows, particle tracking velocimetry experiments are planned in straight channels of typical width 150 μm [49]. Indeed in such microfluidic flows, confinement and the absence of curvature are expected to delay the occurrence of instabilities.

Moreover our data have revealed the presence of wall slip in the thermodynamic nematic phase under shear (Sec. III). Although the presence of three-dimensional flow in the isotropic phase at 41 °C complicates a reliable study of slip velocities, wall slip was also reported in previous experiments performed at 44 °C [26]. Understanding the structure of the slip layers and their dynamics seems like a major challenge from both the experimental and theoretical points of view. To illustrate the complexity of wall slip effects, preliminary experiments were performed where the surface roughness of the cell walls was varied. Figure 16 compares the spatiotemporal diagrams of $\dot{\gamma}(x,t)$ recorded in a smooth Plexiglas Couette cell and in a sand-blasted Couette cell of the same dimensions in our CTAB-D_2O system at 44 °C within the stress plateau region (at $\dot{\gamma}=400\ s^{-1}$). A modification of the boundary conditions significantly influences the nature of the fluctuations: the large periodic oscillations of the position of the interface between shear bands recorded in the smooth geometry are replaced by smaller and erratic fluctuations in the rough Couette cell, where an unstable highly sheared band is also detected several times in the vicinity of the stator [see the white patches in $\dot{\gamma}(x,t)$ for $x\geqslant 0.7$ mm and $t=50$–200 s or $t=900$–1200 s in Fig. 16(b)].

Finally theoretical approaches have proposed that one of the variables of the system involved in the constitutive rheological equation fluctuate in time [50,51]. This variable reflects the local structure of the fluid and can be the Maxwell relaxation time or the mean length of the micelles. Such a phenomenological approach allows one to predict oscillations of the flow field and even chaotic behaviors. Very recently a linear stability analysis was performed on a planar shear-banded flow in the framework of the nonlocal Johnson-Segalman model, that showed the possibility of unstable flows [52]. However, although very informative, neither the linear stability approach nor the subsequent nonlinear numerical calculations [53] can account for three-dimensional flows due to their intrinsic two-dimensional nature. Thus three-dimensional calculations are needed to get a complete picture of the stability of shear-banded flows. Last, our results have emphasized the importance of wall slip. Taking into account the rheology of the slip layers and possible instabilities in the vicinity of the walls (e.g., similar to a stick-slip instability) may shed light on whether wall slip may govern (or at least couple to) the fluctuations observed in the bulk.

VI. CONCLUSION

In this work we have presented a comprehensive study of the CTAB-D_2O system. By simultaneously performing velocimetry and global rheological measurements, we have shown that the flow dynamics becomes very slow along the stress plateau. Consequently, unless very long waiting times of several hours are used [26], the classical, stationary shear-banding scenario of Ref. [13] cannot describe our data. Moreover the flow is characterized by rich and complex dynamics on shorter time scales ranging from 3 to 100 s, which may partly be attributed to the occurrence of a three-dimensional flow. Note that fluctuations faster than 3 s may be present but were not studied with the present version of the velocimetry technique. The analysis of such dynamics is left for future work.

We further argued that the presence of a three-dimensional flow can lead to the detection of an apparently unsheared band in the time-averaged velocity profiles similar to that described by Fischer and Callaghan and interpreted in terms of a "nematic gel" in Ref. [20]. In our opinion the three-dimensional nature of the flow has led to a misinterpretation of the previous experiments in terms of a "nematic gel." We have shown that both an instability of the interface similar to that of Ref. [39] and an elastic instability may account for three-dimensional flows in our sample. Further work dealing with two-dimensional imaging of the flow and microfluidics will be undertaken in the near future to thoroughly check our conclusions. Finally we demonstrated that wall slip strongly influences the nature of the interface fluctuations, and that it should be taken into account in any modeling of the bulk dynamics.

ACKNOWLEDGMENTS

The authors wish to thank A. Aradian, S. Fielding, and P. Olmsted for fruitful discussions. The referees are also thanked for their insightful remarks and criticisms about our manuscript. This work was funded by CNRS, Université Bordeaux 1, and Région Aquitaine. Financial support from the SoftComp European network is also acknowledged.

[1] O. Diat, D. Roux, and F. Nallet, J. Phys. II **3**, 1427 (1993).
[2] L. Ramos, F. Molino, and G. Porte, Langmuir **16**, 5846 (2000).
[3] L. B. Chen, M. K. Chow, B. J. Ackerson, and C. F. Zukoski, Langmuir **10**, 2917 (1994).
[4] G. Waton, B. Michels, A. Steyer, and F. Schosseler, Macromolecules **37**, 2313 (2004).
[5] J.-F. Berret, in *Molecular Gels*, edited by P. Terech and R. Weiss (Elsevier, Amsterdan, 2005).
[6] J.-B. Salmon, A. Colin, S. Manneville, and F. Molino, Phys. Rev. Lett. **90**, 228303 (2003).
[7] Y. T. Hu and A. Lips, J. Rheol. **49**, 1001 (2005).
[8] P. Pimenta and E. E. Pashkovski, Langmuir **22**, 3980 (2006).
[9] J.-F. Berret, D. Roux, G. Porte, and P. Lindner, Europhys. Lett. **25**, 521 (1994).
[10] E. Cappelaere, J.-F. Berret, J.-P. Decruppe, R. Cressely, and P. Lindner, Phys. Rev. E **56**, 1869 (1997).
[11] H. Rehage and H. Hoffmann, Mol. Phys. **74**, 933 (1991).
[12] M. E. Cates, Macromolecules **20**, 2289 (1987).
[13] N. A. Spenley, M. E. Cates, and T. C. B. McLeish, Phys. Rev. Lett. **71**, 939 (1993).
[14] R. B. Bird, R. C. Armstrong, and O. Hassager, *Dynamics of Polymeric Liquids* (Cambridge University Press, Cambridge, 1987).
[15] P. D. Olmsted and C.-Y. D. Lu, Phys. Rev. E **56**, R55 (1997).
[16] J. K. G. Dhont, Phys. Rev. E **60**, 4534 (1999).
[17] J. L. Goveas and P. D. Olmsted, Eur. Phys. J. E **6**, 79 (2001).
[18] X.-F. Yuan and L. Jupp, Europhys. Lett. **60**, 691 (2002).
[19] E. Fischer and P. T. Callaghan, Europhys. Lett. **50**, 803 (2000).
[20] E. Fischer and P. T. Callaghan, Phys. Rev. E **64**, 011501 (2001).
[21] W. M. Holmes, M. R. López-González, and P. T. Callaghan, Europhys. Lett. **64**, 274 (2003).
[22] M. R. López-González, W. M. Holmes, P. T. Callaghan, and P. J. Photinos, Phys. Rev. Lett. **93**, 268302 (2004).
[23] S. Lerouge, J.-P. Decruppe, and C. Humbert, Phys. Rev. Lett. **81**, 5457 (1998).
[24] S. Lerouge, J.-P. Decruppe, and J.-F. Berret, Langmuir **16**, 6464 (2000).
[25] S. Lerouge, J.-P. Decruppe, and P. Olmsted, Langmuir **20**, 11355 (2004).
[26] L. Bécu, S. Manneville, and A. Colin, Phys. Rev. Lett. **93**, 018301 (2004).
[27] S. Manneville, L. Bécu, and A. Colin, Eur. Phys. J.: Appl. Phys. **28**, 361 (2004).
[28] T. Narayanan, O. Diat, and P. Bösecke, Nucl. Instrum. Methods Phys. Res. A **467-468**, 1005 (2001).
[29] P. Panine, M. Gradzielski, and T. Narayanan, Rev. Sci. Instrum. **74**, 2451 (2003).
[30] J.-F. Berret and D. C. Roux, J. Rheol. **39**, 725 (1995).
[31] P. Moldenaers and J. Mewis, J. Rheol. **30**, 567 (1986).
[32] H. A. Barnes, J. Non-Newtonian Fluid Mech. **56**, 221 (1995).
[33] The preferential orientation of the micelles in the velocity direction observed at rest is due to a preshearing step applied to the sample at $\dot{\gamma}=10\ s^{-1}$. The sample was then left at rest at least 15 min before recording the spectrum.
[34] D. C. Roux, J.-F. Berret, G. Porte, E. Peuvrel-Disdier, and P. Lindner, Macromolecules **28**, 1681 (1995).
[35] J.-F. Berret, Langmuir **13**, 2227 (1997).
[36] S. Lerouge, M. Argentina, and J. P. Decruppe, Phys. Rev. Lett. **96**, 088301 (2006).
[37] M. R. López-González, W. M. Holmes, P. T. Callaghan, and P. Photinos, Soft Matter **2**, 855 (2006).
[38] D. J. Tritton, *Physical Fluid Dynamics* (Oxford Science, Oxford, 1988).
[39] F. Charru and P. Barthelet, Physica D **125**, 311 (1999).
[40] E. Hinch, J. Fluid Mech. **144**, 463 (1984).
[41] S. J. Muller, R. G. Larson, and E. S. G. Shaqfeh, Rheol. Acta **28**, 499 (1989).
[42] R. G. Larson, E. S. G. Shaqfeh, and S. J. Muller, J. Fluid Mech. **218**, 573 (1990).
[43] E. Shaqfeh, Annu. Rev. Fluid Mech. **28**, 129 (1996).
[44] K. Weissenberg, Nature (London) **159**, 310 (1947).
[45] M. D. Graham, J. Fluid Mech. **360**, 341 (1998).
[46] G. H. McKinley, P. Pakdel, and A. Öztekin, J. Non-Newtonian Fluid Mech. **67**, 19 (1996).
[47] P. Pakdel and G. H. McKinley, Phys. Rev. Lett. **77**, 2459 (1996).
[48] L. Sandrin, S. Manneville, and M. Fink, Appl. Phys. Lett. **78**, 1155 (2001).
[49] G. Degré, P. Joseph, P. Tabeling, S. Lerouge, M. Cloitre, and A. Ajdari, Appl. Phys. Lett. **89**, 024104 (2006).
[50] S. M. Fielding and P. D. Olmsted, Phys. Rev. Lett. **92**, 084502 (2004).
[51] A. Aradian and M. E. Cates, Europhys. Lett. **70**, 397 (2005).
[52] S. M. Fielding, Phys. Rev. Lett. **95**, 134501 (2005).
[53] S. M. Fielding and P. D. Olmsted, Phys. Rev. Lett. **96**, 104502 (2006).